Strongly anisotropic antiferromagnetic coupling in EuFe₂As₂ revealed by stress detwinning

Joshua J. Sanchez [1,*] Gilberto Fabbris [2] Yongseong Choi [2] Yue Shi [1] Paul Malinowski [1] Shashi Pandey [3] Jian Liu,[3] I. I. Mazin,[5] Jong-Woo Kim,[2] Philip Ryan,[2,4] and Jiun-Haw Chu[1,†]

[1]*Department of Physics, University of Washington, Seattle, Washington 98195, USA*
[2]*Advanced Photon Source, Argonne National Laboratories, Lemont, Illinois 60439, USA*
[3]*Department of Physics and Astronomy, University of Tennessee, Knoxville, Tennessee 37996, USA*
[4]*School of Physical Sciences, Dublin City University, Dublin 9, Ireland*
[5]*Department of Physics and Astronomy and Quantum Science and Engineering Center, George Mason University, Fairfax, Virginia 22030, USA*

Of all parent compounds of iron-based high-temperature superconductors, EuFe₂As₂ exhibits by far the largest magnetostructural coupling due to the sizable biquadratic interaction between Eu and Fe moments. While the coupling between Eu antiferromagnetic (AFM) order and Fe structural/AFM domains enables rapid field detwinning, this prevents simple magnetometry measurements from extracting the critical fields of the Eu metamagnetic transition. Here, we measure these critical fields by combining x-ray magnetic circular dichroism spectroscopy with *in situ* tunable uniaxial stress and applied magnetic field. The combination of two tuning knobs allows us to separate the stress detwinning of structural domains from the field-induced reorientation of Eu moments. Intriguingly, we find a spin-flip transition which can only result from a strongly anisotropic interaction between Eu planes. We argue that this anisotropic exchange is a consequence of the strong anisotropy in the magnetically ordered Fe layer, which presents a form of higher-order coupling between Eu and Fe magnetism.

I. INTRODUCTION

Magnetism is the origin of a wide range of intriguing phenomena in iron-based superconductors, including electronic nematicity and high-temperature superconductivity [1–5]. In contrast to the magnetism of the high-T_c cuprates, the stripe spin density wave (SDW) ground state breaks fourfold rotational symmetry, and the spin dynamics are highly anisotropic [6–9]. Key to this highly anisotropic magnetism is a sizable biquadratic coupling that is not captured in a simple Heisenberg model and likely arises from the dual itinerant-localized character of the Fe magnetism [10,11]. It has also been suggested that this biquadratic term is necessary for the emergence of spin nematicity [12,13].

Very recently, it was shown that a similar biquadratic coupling plays a role in the unusually large magnetoelastic coupling in EuFe₂As₂, where the introduction of a magnetic lanthanide element adds another layer of complexity into the magnetism of iron-based superconductors [14]. In addition to the SDW order, EuFe₂As₂ also hosts an A-type layered antiferromagnetic (AFM) order in the Eu layer, sharing the same easy axis with the Fe SDW. Like in other iron pnictides, the SDW in EuFe₂As₂ creates orthorhombic twin domains. In BaFe₂As₂, due to the strong coupling between the structural distortion and the SDW, an applied field of order 25 T can fully detwin the structural domains [15]. Surprisingly, EuFe₂As₂ can be fully detwinned with <1 T, and

partial detwinning can persist even after the field is turned off [16,17]. Magnetization, nuclear magnetic resonance (NMR), and neutron diffraction data show that this structural detwinning coincides with the reorientation of Eu moments toward the applied field direction, suggesting that the Eu magnetism and the associated large magnetic moments are responsible for this drastic reduction of detwinning field [16,18,19]. Nevertheless, as no single-ion anisotropy is present for the half-filled Eu $4f^7$ electrons and no dipolar coupling between the Fe and Eu layers is allowed by symmetry, it remained an open question how Eu moments even sense the orthorhombic direction. Recently, Maiwald *et al.* [14] solved this mystery by considering a biquadratic coupling between Fe SDW and Eu AFM moments. The biquadratic coupling of the form $K(\boldsymbol{f}_i \cdot \boldsymbol{e}_j)^2$, where $\boldsymbol{f}_i$ and $\boldsymbol{e}_j$ represent the Fe and Eu moments, respectively, provides an effective single-ion anisotropy that couples the Eu moment orientation with the Fe SDW direction [14]. Therefore, while the Fe-Fe biquadratic coupling generates the nematicity in the FeAs layer, the Eu-Fe biquadratic coupling provides a pathway for the Eu magnetism to couple to the structural orthorhombicity and the underlying nematicity.

Here, we report the discovery of another consequence of the higher-order Eu-Fe coupling in EuFe₂As₂—a highly anisotropic Eu-Eu interplanar coupling. The degree of anisotropy of Eu-Eu interlayer exchange ($\frac{J_x - J_y}{J_x + J_y}$) is ∼75 times larger than the structural orthorhombicity, which can only be understood by considering the influence of the Fe SDW order. The anisotropy of Eu-Eu interlayer exchange was overlooked previously because the field detwinning process masked the

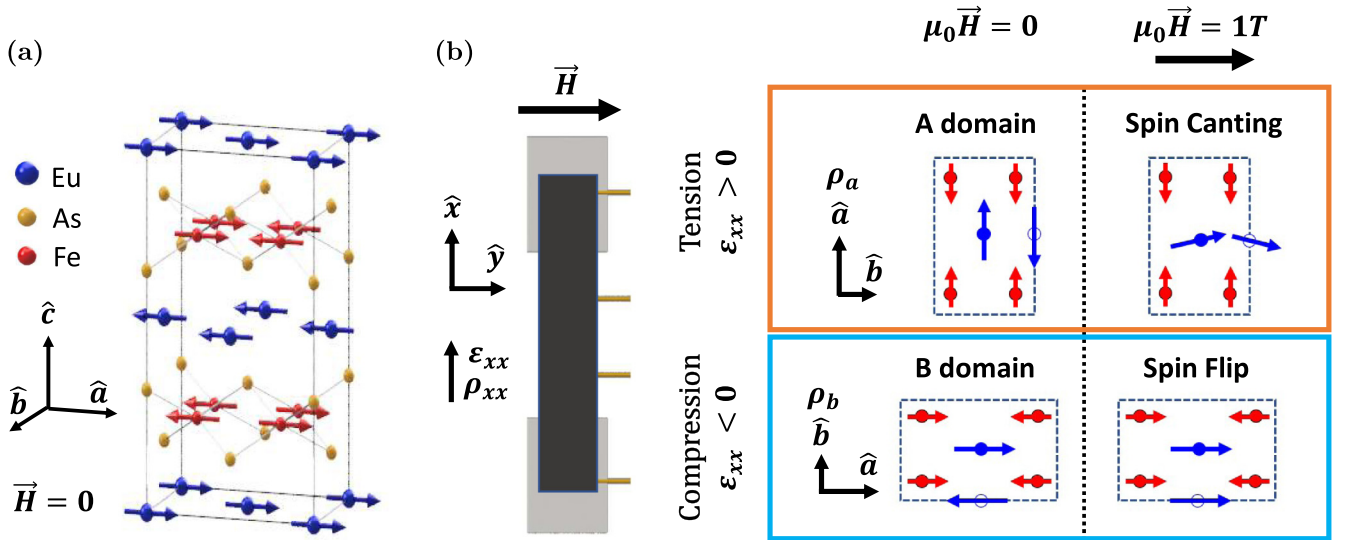*Corresponding author: jjsanchez2012@gmail.com
†jhchu@uw.edu

FIG. 1. (a) EuFe$_2$As$_2$ unit cell at $T = 7$ K and zero applied magnetic field. Both Fe and Eu antiferromagnetic orders are stabilized with easy axes aligned with the longer a lattice constant of the orthorhombic unit cell. (b) Uniaxial stress is applied along the $\hat{x}$ direction aligned with the orthorhombic a/b orthorhombic unit cell lattice directions such that tension (compression) detwins the sample to the A (B) domain (orange/blue outline). Resistivity measurements along the stress axis measure ρ_a (ρ_b) aligned with the a (b) lattice constant of the A (B) domain. A magnetic field is applied perpendicular to the strain axis at $10°$ above parallel from the a/b plane, causing a reorientation of Eu moments to align along the field direction. XMCD is proportional to the Eu magnetization along the applied field direction. For simplicity, we collapse the 4 Eu atoms and 8 Fe atoms of the doubled orthogonal unit cell into 2 Eu (blue arrows) and 4 Fe (red arrows) effective moments.

spin-flip nature of Eu metamagnetic transition. We overcome this challenge by a direct measurement of the Eu metamagnetic transition in a mechanically detwinned sample using a piezoelectric stress device, which allows us to apply magnetic fields either parallel or perpendicular to the easy axis of Eu moments within a single structural domain. Conventional magnetometry techniques are difficult to apply to a sample mounted to a strain device due to the added size and background magnetization contributed by the device. We therefore employ x-ray magnetic circular dichroism (XMCD) on the Eu L_3 edge to measure the Eu-specific in-plane magnetization induced by an applied magnetic field. We show that we can strain the crystal into a monodomain which exhibits either a large jump in magnetization, consistent with a spin-flip transition, or has a perfectly linear magnetization from continuous canting of Eu moments (i.e., we are able to turn the metamagnetic transition on and off). From the measurement of the critical field for the Eu spin flip and the field dependence of the spin canting, we determine the energies of the Eu-Eu and Eu-Fe coupling and discover that the Eu-Eu interaction itself is directionally dependent on the orientation of Fe moments. We then confirm this by first-principles calculations. The discovery of the anisotropic Eu-Eu interplanar coupling also sheds light on the evolution of the Eu magnetism in doped EuFe$_2$As$_2$, which we reevaluate in the discussion. Finally, simultaneous transport measurements suggest a unique Eu origin of the large magnetoresistance jump previously found in the system [17,20].

II. RESULTS

Figure 1(a) shows the fully magnetically ordered unit cell at $T = 7$ K and zero applied magnetic field. Eu moments

are aligned ferromagnetically within each plane and antiferromagnetically between planes. The Fe SDW ordering results in a small structural orthorhombicity and the formation of structural twin domains that are identical up to a $90°$ rotation. Within each domain, the Eu AFM and Fe SDW easy axes are aligned with the longer orthorhombic a lattice constant [21,22]. We use a geometry with the $\hat{x}$ and $\hat{y}$ axes aligned to the orthorhombic a and b directions, and tensile or compressive stress applied along the $\hat{x}$ direction detwins the sample toward the A monodomain (a lattice vector along $\hat{x}$) or B monodomain (b lattice vector along $\hat{x}$), respectively [Fig. 1(b)]. Given the maximum orthorhombicity of EuFe$_2$As$_2$ (0.28% at 2.5 K [22]) and the maximum strain of the sample device at 7 K (0.3%), we are capable of nearly fully detwinning the sample (the minor domain is estimated to be 5% or less of the sample volume, see Fig. S2 in the Supplemental Material [23] and Ref. [24]). Once in the A (B) monodomain state, the measured resistivity ρ_{xx} becomes sensitive to the anisotropic resistivity ρ_a (ρ_b) along the orthorhombic a (b) direction. Magnetic field is applied perpendicular to the current/strain axis and at $10°$ above the ab plane. Except for a change in the strain state, the sample is not reoriented in any way during the experiment, ensuring identical effective fields and XMCD-illuminated sample volumes. XMCD measures the induced Eu magnetic moment along the field direction, which is fixed parallel to the incident x-ray direction in this paper.

First, we address the effect of the applied magnetic field at $T = 30$ K, below the orthorhombic and SDW transitions ($T_{SDW} = 187$ K) but above the Eu AFM ordering temperature ($T_N = 19.1$ K). In the Eu^{2+} valence state, the $4f^7$ electrons have zero orbital angular momentum ($L = 0$) and as such are expected to show an isotropic response to applied field. After
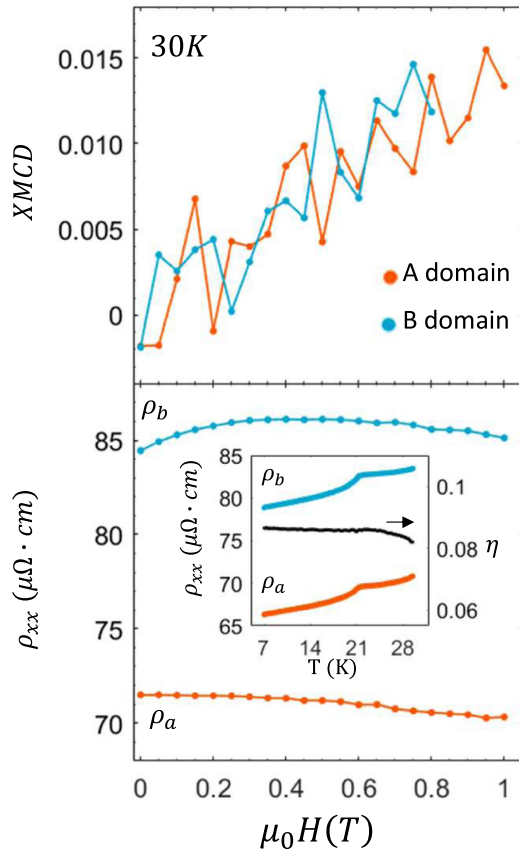
FIG. 2. $T = 30$ K single pass applied magnetic field sweep for the detwinned A and B domains [XMCD data were not collected for B domain 0.8–1 T]. XMCD above the Eu antiferromagnetic (AFM) ordering temperature shows a nearly isotropic response to field. ρ_{xx} vs applied magnetic field reveals a minimal magnetoresistance. (Inset, left) ρ_{xx} vs temperature for the detwinned A and B monodomains reveal no additional anisotropy induced at the Eu AFM ordering temperature $T_{N,\text{Eu}} = 19.1$ K. (Inset, right) The resistivity anisotropy $\eta = \frac{\rho_b - \rho_a}{\rho_b + \rho_a}$ (black).

detwinning to either the A or B monodomain, we applied fields from 0 to 1 T and measured the XMCD and resistivity simultaneously in 0.02 T steps (XMCD data were not collected for the B monodomain for 0.8–1 T at this temperature). We find an XMCD signal that is indistinguishable between the two domains, suggesting that, at this temperature and field range, the Eu-Fe interaction is negligible compared with the Eu paramagnetic coupling to applied field (Fig. 2). We note that, compared with the data presented next, the XMCD values at 1 T and 30 K are roughly 3 times smaller than the 1 T XMCD saturation value within the Eu AFM phase, consistent with a lower susceptibility in the paramagnetic phase. As in BaFe$_2$As$_2$, the zero-field resistivity is considerably larger along the orthorhombic b direction than the a direction [25–27]. Both ρ_a and ρ_b have a weak field dependence at 30 K. The inset to Fig. 2 shows the detwinned sample cooling through the Eu AFM transition. As demonstrated previously in mechanically detwinned EuFe$_2$As$_2$, we see no change in the Eu transition temperature between the tensile and compressive cooling data, nor do we see any additional resistivity anisotropy induced by the Eu AFM ordering [28]. Indeed, the

resistivity anisotropy $\frac{\rho_b - \rho_a}{\rho_b + \rho_a} = 0.084(2)$ is unchanged through this temperature range.

We now discuss results from within the Eu AFM phase at 7 K. We applied field through a ± 1 T loop to each detwinned state and measured the XMCD and resistivity simultaneously in 0.02 T steps (Fig. 3). In the A domain [Fig. 3(a)], the Eu moments are initially aligned with the AFM easy axis transverse to the field direction. The linear growth of XMCD signal with field indicates that Eu moments cant continuously to align with the field, with no observable hysteresis. Conversely, in the B domain [Fig. 3(b)], the easy axis is along the field direction, and so for fields <0.4 T, the XMCD is nearly flat, as no canting can occur. The jump in XMCD from 0.4 to 0.6 T and accompanying hysteresis is a clear sign of a metamagnetic spin-flip transition between the Eu AFM and ferromagnetic (FM) states. The weak linear field dependence of magnetization in the pre- and post-spin-flip field ranges are due to the out-of-plane magnetization induced by the small out-of-plane field component, which is assumed to equally contribute to the A domain magnetization. We note that the observation of spin-flip transition contradicts the expectation from the spin Hamiltonian derived from Ref. [14], which predicts a spin-flop transition. As will be shown in the Discussion section, this contradiction can only be resolved by including an anisotropic interlayer exchange between Eu moments.

The resistivity is approximately linear in field for $|\mu_0 H| <$ 0.4 T and $|\mu_0 H| > 0.6$ T for both domains. For 0.4 T $< |\mu_0 H| < 0.6$ T, a large hysteretic drop occurs in the B domain resistivity, coinciding with the jump in XMCD. A much smaller drop also occurs in the A domain, which also shows a small hysteresis [Fig. 3(a), inset] and is likely due to a remnant B domain that was not fully detwinned and which is not resolved in the XMCD measurement. For each domain, the resistivity returns to the initial zero-field value after the field loop, indicating that there is no persistent field detwinning in our setup, as is found reliably from previous studies of free-standing samples [16,17]. Further, given the field and current orientation, the sample in either strain state would be expected to detwin toward the higher-resistivity B domain >~0.5 T, and so the drop in resistivity for both domains suggests that our stress device is indeed preventing field detwinning. This is also strong evidence for a purely Eu spin origin of the resistivity jump.

Both the XMCD and resistivity data show excellent agreement between positive and negative field values. In Fig. 4(a), we plot the average value over positive and negative field sweeps of the XMCD and the magnetoresistance. While we were unable to apply enough field to fully saturate the A domain XMCD, we can extrapolate the field dependencies of each domain to estimate the saturation field. Linear fits to the XMCD of the A and B domains at fields >0.6 T are shown, with an intersection at $\mu_0 H_A^{\text{sat}} = 1.17$ T. Beyond this field, the Eu magnetic moment is expected to be fully saturated in each domain, as seen in freestanding crystal magnetometry studies [14,17,18,29]. To more precisely determine the B domain spin-flip field H_B^{flip}, we use the value at the center of the field hysteresis. Figure 4(b) shows the difference between the increasing and decreasing field values of the XMCD and resistivity. In the B domain, a sharp peak in both quantities
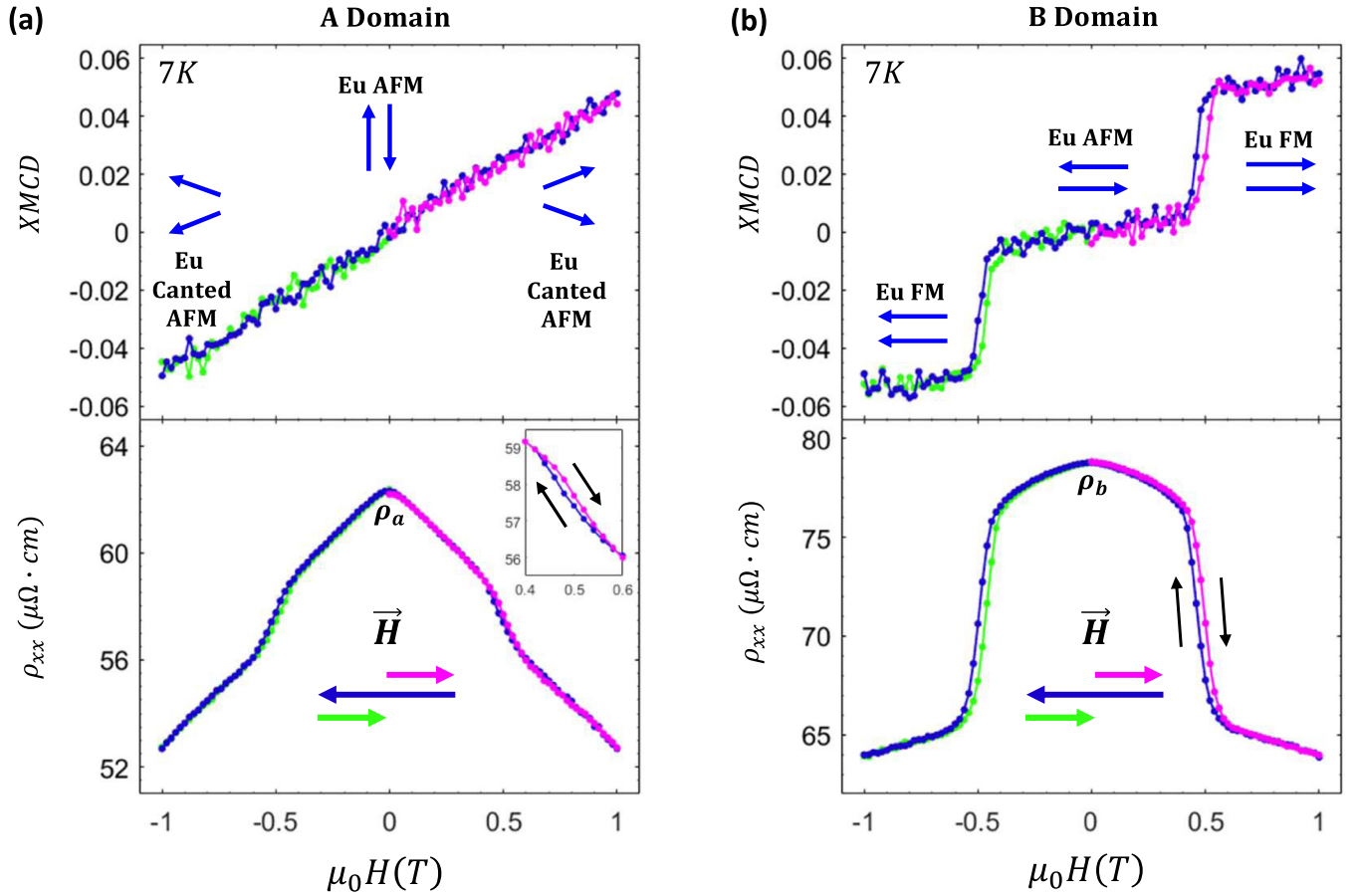
FIG. 3. Field sweep at $T = 7$ K in the fully magnetically ordered phase presented in Fig. 1(a). Applied field ramped from 0 to 1, -1, and 0 T in each detwinned (a) A and (b) B monodomain states. Inset to bottom panel of (a) shows the small magnetoresistance hysteresis visible ~ 0.5 T in the A domain.

occurs at $\mu_0 H_B^{\text{flip}} = 0.48$ T. In principle, the lattice distortions induced by the detwinning strain could cause a change in the interaction strengths between Eu and Fe planes that could alter these critical fields. In Fig. S3 in the Supplemental Material [23], we present data for the same sample tuned to a nearly zero strain state in which both A and B domains are present and show that H_A^{sat} and H_B^{flip} are essentially unchanged, demonstrating that the strain applied to detwin the sample does not appreciably affect the interplanar coupling strengths.

III. DISCUSSION

We can relate the spin-flip and saturation fields H_B^{flip} and H_A^{sat} to the microscopic interactions in the sample using a spin Hamiltonian (Section IV of Supplemental Material [23]). We will start with a modified version of the spin Hamiltonian presented in Ref. [14] and show that, to explain the experimental results, an additional anisotropic exchange term is needed. We consider first a purely isotropic exchange energy $2J$ between Eu AFM planes in the doubled unit cell of the fully ordered state (Eu$_2$Fe$_4$As$_4$). From the symmetry of the magnetic ordering structure [Fig. 1(a)], the dipolar interactions of Eu and Fe moments cancel each other and so do not contribute to the magnetic energy. The half-filled $4f^7$ orbital of Eu^{2+} has zero orbital angular momentum ($L = 0$) and negligible single-ion anisotropy, but the posited biquadratic coupling between

Eu and Fe moments creates an effective magnetocrystalline anisotropy. We define a biquadratic coupling energy K between the eight inequivalent Eu-Fe moment pairs, with a total Eu-Fe planar coupling energy $8K$. Following the usual treatment of spin-flip and spin canting transitions, we determine the critical fields as

$$H_B^{\text{flip}} = \frac{2J}{M}, \quad H_A^{\text{sat}} = \frac{4J + 16K}{M} = 2\left(H_B^{\text{flip}} + \frac{8K}{M}\right).$$

For the B domain, Eu and Fe moments are aligned both before and after the spin flip, and so the presence of the biquadratic coupling does not change the value of the spin-flip field but only serves to provide the necessary magnetocrystalline anisotropy to enforce a sharp spin-flip transition. For the A domain, the biquadratic coupling provides an extra energy barrier that must be overcome by the field to reach the fully saturated canted state. From the measured values $\mu_0 H_A^{\text{sat}} = 1.17$ T and $\mu_0 H_B^{\text{flip}} = 0.48$ T, and using the expected Eu moment $M = 6.8\,\mu_B$ [16,17], we obtain $J = 94.5\,\mu$eV and $8K = 41.3\,\mu$eV. Thus, the Eu-Eu and Eu-Fe planar coupling energies are comparable, with $\frac{J}{8K} = 2.3$.

At this point, we are facing an apparent contradiction: we observe experimentally a sharp spin-flip transition, but for $\frac{J}{8K} > 1$, the spin Hamiltonian would be expected to result in a spin-flop transition, as shown in Fig. 5(a) (see Ref. [14] and Section IV of Supplemental Material [23] for
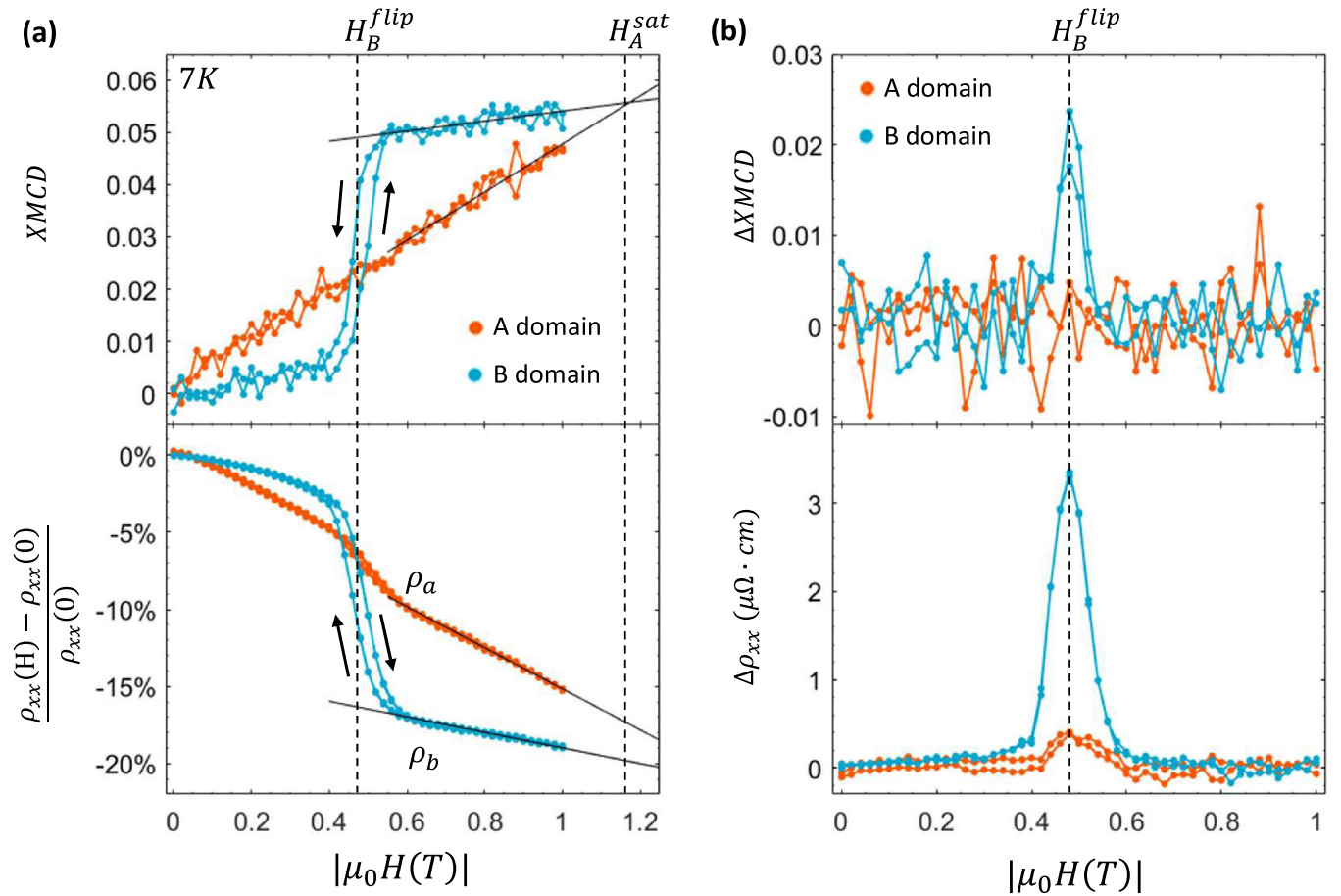
FIG. 4. (a) Data from Figs. 3(a) and 3(b) replotted as the average value of positive and negative field sweeps of XMCD and the magnetoresistance against the absolute value of applied magnetic field for the detwinned A (orange) and B (blue) monodomains. Linear fits (black lines) to the XMCD magnitude for $|\mu_0 H| = 0.6$ T to 1 T indicate both values coincide at $|\mu_0 H_A^{sat}| \sim 1.17$ T. The magnetoresistance for positive and negative field are nearly identical and tightly overlap. (b) The difference in XMCD and ρ_{xx} for increasing and decreasing fields yields $\Delta XMCD = XMCD(H_{inc}) - XMCD(H_{dec})$ and $\Delta\rho_{xx} = \rho_{xx}(H_{inc}) - \rho_{xx}(H_{dec})$. For the B domain, the peak values of $\Delta XMCD$ and $\Delta\rho_{xx}$ coincide at $\mu_0 H_B^{flip} = 0.48$ T.

further discussion). This discrepancy has important implications for correctly modeling the field detwinning process, which has been based on the (never actually observed) spin-flop transition. This apparent contradiction indicates that an additional term is needed in the spin Hamiltonian. The simplest such term is a symmetric anisotropic exchange term $W(e_{i,x}e_{i+1,x} - e_{i,y}e_{i+1,y})$, where $e_{i,x}$ and $e_{i,y}$ are the x and y components of the Eu moment in the ith layer, using a notation with Fe moments aligned antiferromagnetically along $\hat{x}$. This term then increases (decreases) the interaction strength between Eu moments when aligned parallel (perpendicular) to the Fe moments and provides the additional anisotropy needed to enforce a spin-flip transition. Although other higher-order terms could also be introduced to the spin Hamiltonian, they generally lead to nonlinear M-H curves which were not observed in the experiment. With this additional term, the criterion for a spin-flip transition becomes $\frac{J}{8K+W} < 1$, and the critical fields are

$$H_B^{flip} = \frac{2(J+W)}{M},$$

$$H_A^{sat} = \frac{4J + 16K}{M} = 2\left(H_B^{flip} + \frac{8K - 2W}{M}\right).$$

The three parameters J, K, and W cannot be uniquely determined by the two experimentally measured values. Therefore, additional constraint is needed. This constraint can be provided by the measurement of $H_{45°}^{sat}$, i.e., the field required to saturate the magnetization when the field is aligned 45° to the easy and hard axis, such that the field has an equivalent effect on both domains. It has the following expression:

$$H_{45°}^{sat} = \frac{4J}{M}.$$

As our strain + XMCD measurements have demonstrated the need for the W term, we now discuss the extraction of J, K, and W from magnetization measurements using a vibrating sample magnetometer (VSM) on a second sample from the same growth batch. We stress that this extraction is not possible without the confirmation of a spin-flip transition by XMCD measurement on a stress-detwinned sample. The sample was encased in GE varnish so that the domain configuration is fixed to 50/50 and the field detwinning is prohibited. The thin octagonal shape of the sample also ensures that field applied totally in plane along the $[1 0 0]_T$ and $[1 1 0]_T$ directions have an identical (negligible)
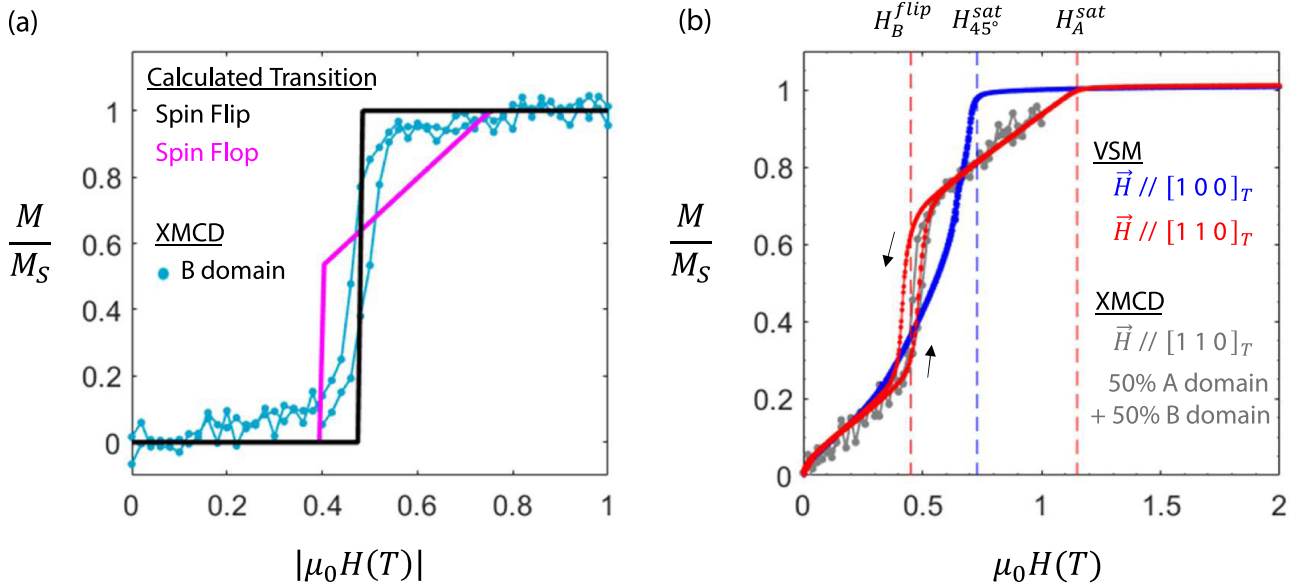
FIG. 5. (a) XMCD data of Fig. 4(a) for the B domain normalized to the 1 T mean value. Black (magenta) line represents the $T = 0$ K metamagnetic spin flip (spin flop) transition calculated using the anisotropic JKW (isotropic JK) model (see main text). (b) Octagon sample magnetization with field applied along the tetragonal $[1\,0\,0]_T$ (blue) and $[1\,1\,0]_T$ (red) directions. Critical fields marked by dashed lines. Magnetization normalized by 1 T saturation value along $[1\,0\,0]_T$ (gray). Average of the two domain XMCD data of Fig. 4(a), normalized by the B domain saturated value at 1 T.

demagnetization factor (see Methods). As shown in Fig. 5(b), at $T = 2$ K for field applied along the $[1\,0\,0]_T$ direction (blue curve), i.e., at $45°$ to both domain easy axes, the magnetization exhibits continuous spin canting toward saturation at $\mu_0 H_{45°}^{sat} = 0.73$ T. For field applied along the $[1\,1\,0]_T$ direction (red curve), the M vs H perfectly overlaps with the combination of the responses of A and B domains from the XMCD measurements (gray), confirming the absence of field detwinning. We extract $\mu_0 H_A^{sat} = 1.15$ T and $\mu_0 H_B^{flip} = 0.45$ T from these spin-flip and saturation fields, which is in good agreement with the XMCD-measured values. Using these three measured values, we can uniquely solve for the interaction terms and find $J = 71.8$ μeV, $W = 16.7$ μeV and $8K = 82.7$ μeV, with a ratio $\frac{J}{8K+W} = 0.72 < 1$ satisfying the sharp spin-flip criterion. Therefore, we find that the Eu-Eu interaction is much stronger for Eu moments aligned parallel ($J_x = J + W = 88.5$ μeV) than perpendicular ($J_y = J - W = 55.1$ μeV) to Fe moments. Further, the normalized difference of the anisotropic interplanar interaction $\frac{J_x - J_y}{J_x + J_y} = 23.3\%$ is nearly two orders of magnitude greater than the corresponding normalized difference of in-plane lattice constants (the orthorhombicity) $\frac{a-b}{a+b} \sim 0.28\%$, which strongly implies the Fe SDW origin of the anisotropy.

To gain more insight, we used density functional theory (DFT) to calculate the exchange coupling between Eu layers as the difference between ferromagnetically and antiferromagnetically stacked Eu layers, for Eu moments parallel and perpendicular to the Fe moments. We used the standard VASP package [30,31] and verified that the results were fully converged with respect to the Brillouin zone integration, plane-wave cutoff, and the number of bands included in the diagonalization. We also varied the effective Hubbard repulsion parameter for Eu f orbitals $U - J$ between 5 and

7 eV, which had little impact on the result. We find that for parallel Eu-Fe moments $J_x = 150 - 170$ μeV, while for perpendicular Eu-Fe moments, J_y is essentially zero. While this result seems to considerably overestimate the exchange anisotropy (see Ref. [14], Supplemental Material Sec. 1A, for a discussion of the difficulties of DFT calculation for noncollinear Eu-Fe moments, which we assume contributes to this overestimation), it clearly shows that DFT calculations also support a strongly anisotropic Eu interplanar interaction.

The anisotropic interaction between Eu planes can be thought to result from the anisotropic hopping of conduction electrons through the Fe plane. Considering a standard superexchange interaction, conduction electrons with spins polarized along the Eu direction will generally have a larger Eu-Fe hopping amplitude t when the Eu and Fe moments are parallel ($J_x = J + W$) rather than perpendicular ($J_y = J - W$), which generates a stronger AFM interaction for collinear Eu-Fe moments. Further, the weak but finite FM interaction between Eu planes is also mediated through the Fe layer, and as the Fe moments have a much larger susceptibility perpendicular to their ordering direction, the FM interaction is stronger for perpendicular Eu and Fe moments, which weakens their overall effective AFM interaction (this can be considered an extreme case of the Ruderman–Kittel–Kasuya–Yosida (RKKY) interaction). In this sense, we can view this Eu interplanar interaction anisotropy (W) as a generalized Eu-Fe biquadratic coupling independent of the previously investigated Eu-Fe biquadratic coupling (K), where the square of Fe moments ($f_{i,x}^2 - f_{i,y}^2$) couples the Eu moments above and below the iron plane. We note that this picture is reminiscent of the Fe-Fe biquadratic coupling within the FeAs plane that generates an effective anisotropic in-plane exchange of Fe moments $J_{1a} - J_{1b}$ [11]. These types of interactions have been

long overlooked in the past but are relevant to rare-earth and transition metal intermetallic systems with multiple magnetic orders [32,33].

A complete determination of the spin Hamiltonian in $EuFe_2As_2$ also sheds light on the doping dependence of Eu magnetic order, which has yet to be fully understood. As in other iron pnictides, chemical doping in $EuFe_2As_2$ rapidly suppresses the Fe SDW and stabilizes superconductivity [34–42]. In contrast, the doping has only a weak effect on the magnetic ordering temperature in the Eu layer but causes a smooth evolution from an A-type AFM order to a c-axis canted AFM order (c-AFM), and finally to a c-axis FM order [21,22,41–47]. This doping dependence can be naturally understood as the consequence of Eu moments lowering their energy by aligning with the Fe SDW, with this energy saving being gradually diminished as doping weakens the Fe SDW. Further, in the parent compound, both the Fe SDW and Eu AFM are robust under moderate hydrostatic pressure even as superconductivity develops [48], while in the underdoped case, a pressure-induced transition from c-AFM to FM occurs only after the SDW is nearly fully suppressed [49]. This suggests the SDW plays a role in both the orientation and the interaction of Eu moments. Future doping dependence studies may provide more insight on how the Eu interlayer interaction is influenced by the various orders in the FeAs plane, including by superconductivity [50].

In conclusion, our sample environment allows us to approach the magnetic coupling and magnetotransport properties of the $EuFe_2As_2$ system in an unprecedented fashion. Through mechanical stress, we can prevent field detwinning and gain access to the metamagnetism and the associated magnetotransport behavior of a monodomain sample. From measurements of the spin-flip and moment saturation fields, we can determine the strengths of coupling between Eu and Fe planes and discover the presence of an anisotropic exchange term in the spin Hamiltonian. We emphasize again that, in a freestanding crystal, the rapid field detwinning has prevented any previous determination of the anisotropic Eu interplanar interaction in this system. This technique not only deepens our understanding of the $EuFe_2As_2$ system but can also be applied to a variety of systems to disentangle the strongly coupled spin, orbit, and lattice degree of freedom.

IV. METHODS

A. Sample preparation

Single crystal samples of $EuFe_2As_2$ were grown from a tin flux as described elsewhere [43]. The sample was cleaved from a large as-grown single crystal plate and cut along the tetragonal [1 1 0] direction into a bar with dimensions $3.2 \times 0.50 \times 0.065$ mm. These sample dimensions correspond to a demagnetization factor of $N = 0.13$ along the applied field direction [51], resulting in a small maximum demagnetization field of only $NM_{Eu} \sim 0.005$ T. A piezo-actuator uniaxial stress device (Razorbill Instruments, CS-100) was used to provide *in situ* stress in the B_{2g} symmetry channel, i.e., in the direction of the orthorhombic distortion, such that the applied tensile or compressive stress detwins the sample to either the A or B domain, respectively [24,52] (Fig. 1). The

four-wire electrical contact geometry is illustrated in Fig. 1, with wires underneath the sample to not obstruct the x-ray fluorescence off the top surface of the crystal. Measurements of the resistivity coefficient ρ_{xx} aligned along the stress axis were performed using a standard 4-point measurement and an SR830 lock-in amplifier. A second sample from the same growth batch was cut into a thin octagon with surface area 2.18 mm^2 and thickness 0.0165 mm, with negligible in-plane demagnetization factor [51]. Magnetization was measured in a Quantum Design PPMS.

B. XMCD

XMCD was measured at the Advanced Photon Source beamline 4-ID-D at Argonne National Laboratory. We probed the Eu L_3 edge using x rays of 6.97 keV, which measure the spin polarization of the Eu $5d$ band due to the magnetic moment of the $4f$ orbital. Generally, the Eu L_3 edge XMCD signal can be taken as proportional to the $4f$ moment magnetization; however, as the Eu $5d$ band has a significant hybridization with the As $4p$ orbitals [53], which themselves hybridize with the Fe $3d$ orbitals, the exact value of the XMCD is expected to have some dependence on Fe conduction effects. Nonetheless, we can use the sharp changes in XMCD signal to mark the fields at which magnetic transitions and saturations occur. A superconducting split coil magnet with a large bore was used to apply magnetic field. The sample temperature was controlled using He flow. XMCD was collected in fluorescence geometry by monitoring the Eu L_α line using a four-element Vortex detector integrated with the Xspress module to enable a larger dynamical range. Circularly polarized x-rays were generated using a 180-μm-thick diamond (111) phase plate. Data were corrected for self-absorption.

The XMCD spot size illuminates the whole sample width across the y direction and is roughly 100 μm wide along the x direction (between the transport wires) and probes a depth of $\sim$5 μm. The beam is centered on the middle of the crystal where strain is most transmitted and homogenous. The transport wires are separated by $\sim$1700 μm, and transport is sensitive to the whole bulk of the sample [54]. While the resistivity and XMCD are not measuring exactly the same volume of crystal, the tight correlation between the two datasets suggests no major difference in crystal behavior between the two sampled volumes.

C. Magnetization measurement

The magnetization of the single-crystal $EuFe_2As_2$ sample was measured by the VSM option of a Quantum Design Dynacool. The sample was cut into a thin octagon so that field applied along the $[1\,0\,0]_T$ and $[1\,1\,0]_T$ directions has the same (minimal) demagnetization factor. The sample was encased in GE varnish, which is known to fix the domain configuration and prevent field detwinning. In Fig. 5, at $T = 2$ K, the field was applied and magnetization measured along the $[1\,0\,0]_T$ direction (blue), i.e., at 45° to both domain easy axes, and the magnetization indicates a continuous spin canting toward a saturation at $\mu_0 H_{45°}^{sat} = 0.73$ T. Conversely, for field applied along $[1\,1\,0]_T$, the magnetization

appears to be a combination of both a B domain spin flip at $\mu_0 H_B^{flip} = 0.45$ T and an A domain continuous spin canting which saturates at $\mu_0 H_A^{sat} = 1.15$ T, in strong agreement with the detwinned XMCD data of Fig. 4. To further demonstrate this, we normalize the XMCD data of Fig. 4 by the B domain 1 T saturated value and average their values over the field range to simulate a 50/50 perfectly twinned sample. These data are plotted in gray in Fig. 5(b) and are in very strong agreement with the octagonal sample, from which we conclude that the domain populations are indeed held fixed by the GE varnish.

The authors declare that all data supporting the findings of this study are available within this paper or from the corresponding author upon reasonable request.

[1] P. Dai, J. Hu, and E. Dagotto, Nat. Phys. **8**, 709 (2012).

[2] P. Dai, Rev. Mod. Phys. **87**, 855 (2015).

[3] R. M. Fernandes, D. K. Pratt, W. Tian, J. Zarestky, A. Kreyssig, S. Nandi, M. G. Kim, A. Thaler, N. Ni, P. C. Canfield, R. J. McQueeney, J. Schmalian, and A. I. Goldman, Phys. Rev. B **81**, 140501(R) (2010).

[4] F. Kretzschmar, T. Böhm, U. Karahasanović, B. Muschler, A. Baum, D. Jost, J. Schmalian, S. Caprara, M. Grilli, C. Di Castro, J. G. Analytis, J. H. Chu, I. R. Fisher, and R. Hackl, Nat. Phys. **12**, 560 (2016).

[5] M. D. Watson, P. Dudin, L. C. Rhodes, D. V. Evtushinsky, H. Iwasawa, S. Aswartham, S. Wurmehl, B. Büchner, M. Hoesch, and T. K. Kim, Npj Quantum Mater. **4**, 36 (2019).

[6] J. Zhao, D. T. Adroja, D. X. Yao, R. Bewley, S. Li, X. F. Wang, G. Wu, X. H. Chen, J. Hu, and P. Dai, Nat. Phys. **5**, 555 (2009).

[7] S. O. Diallo, V. P. Antropov, T. G. Perring, C. Broholm, J. J. Pulikkotil, N. Ni, S. L. Bud'ko, P. C. Canfield, A. Kreyssig, A. I. Goldman, and R. J. McQueeney, Phys. Rev. Lett. **102**, 187206 (2009).

[8] J. Pelliciari, K. Ishii, M. Dantz, X. Lu, D. E. Mcnally, V. N. Strocov, L. Xing, X. Wang, C. Jin, H. S. Jeevan, P. Gegenwart, and T. Schmitt, Phys. Rev. B **95**, 115152 (2017).

[9] X. Lu, R. Zhang, H. Luo, A. H. Nevidomskyy, Q. Si, and P. Dai, Science. **345**, 657 (2014).

[10] A. N. Yaresko, G. Q. Liu, V. N. Antonov, and O. K. Andersen, Phys. Rev. B **79**, 144421 (2009).

[11] A. L. Wysocki, K. D. Belashchenko, and V. P. Antropov, Nat. Phys. **7**, 485 (2011).

[12] R. M. Fernandes, A. V. Chubukov, J. Knolle, I. Eremin, and J. Schmalian, Phys. Rev. B **85**, 024534 (2012).

[13] J. K. Glasbrenner, I. I. Mazin, H. O. Jeschke, P. J. Hirschfeld, R. M. Fernandes, and R. Valentí, Nat. Phys. **11**, 953 (2015).

[14] J. Maiwald, I. I. Mazin, and P. Gegenwart, Phys. Rev. X **8**, 011011 (2018).

[15] J. P. C. Ruff, J. H. Chu, H. H. Kuo, R. K. Das, H. Nojiri, I. R. Fisher, and Z. Islam, Phys. Rev. Lett. **109**, 027004 (2012).

[16] Y. Xiao, Y. Su, W. Schmidt, K. Schmalzl, C. M. N. Kumar, S. Price, T. Chatterji, R. Mittal, L. J. Chang, S. Nandi, N. Kumar, S. K. Dhar, A. Thamizhavel, and T. Brueckel, Phys. Rev. B **81**, 220406(R) (2010).

[17] S. Zapf, C. Stingl, K. W. Post, J. Maiwald, N. Bach, I. Pietsch, D. Neubauer, A. Löhle, C. Clauss, S. Jiang, H. S. Jeevan, D. N. Basov, P. Gegenwart, and M. Dressel, Phys. Rev. Lett. **113**, 227001 (2014).

[18] S. Jiang, Y. Luo, Z. Ren, Z. Zhu, C. Wang, X. Xu, Q. Tao, G. Cao, and Z. Xu, New J. Phys. **11**, 025007 (2009).

[19] Q.-P. Ding, N. S. Sangeetha, W. R. Meier, M. Xu, S. L. Bud'ko, P. C. Canfield, D. C. Johnston, and Y. Furukawa, Phys. Rev. B **102**, 180406(R) (2020).

[20] Z. Xu, J. Pan, Z. Tao, R. Liu, and G. Tan, Chinese Phys. B **29**, 77402 (2020).

[21] J. Herrero-Martín, V. Scagnoli, C. Mazzoli, Y. Su, R. Mittal, Y. Xiao, T. Brueckel, N. Kumar, S. K. Dhar, A. Thamizhavel, and L. Paolasini, Phys. Rev. B **80**, 134411 (2009).

[22] Y. Xiao, Y. Su, M. Meven, R. Mittal, C. M. N. Kumar, T. Chatterji, S. Price, J. Persson, N. Kumar, S. K. Dhar, A. Thamizhavel, and T. Brueckel, Phys. Rev. B **80**, 174424 (2009).

[23] See Supplemental Material at http://link.aps.org/supplemental/10.1103/PhysRevB.104.104413 for additional XMCD data, modelling of twin domain stress detwinning, and further details of the anisotropic spin Hamiltonian.

[24] J. J. Sanchez, P. Malinowski, J. Mutch, J. Liu, J.-W. Kim, P. J. Ryan, and J.-H. Chu, Nat. Mater. (2021).

[25] R. M. Fernandes, E. Abrahams, and J. Schmalian, Phys. Rev. Lett. **107**, 217002 (2011).

[26] B. Valenzuela, E. Bascones, and M. J. Calderón, Phys. Rev. Lett. **105**, 207202 (2010).

[27] C. C. Chen, J. MacIejko, A. P. Sorini, B. Moritz, R. R. P. Singh, and T. P. Devereaux, Phys. Rev. B **82**, 100504(R) (2010).

[28] J. J. Ying, X. F. Wang, T. Wu, Z. J. Xiang, R. H. Liu, Y. J. Yan, A. F. Wang, M. Zhang, G. J. Ye, P. Cheng, J. P. Hu, and X. H. Chen, Phys. Rev. Lett. **107**, 067001 (2011).

[29] T. Terashima, N. Kurita, A. Kikkawa, H. S. Suzuki, T. Matsumoto, K. Murata, and S. Uji, J. Phys. Soc. Jpn. **79**, 103706 (2010).

[30] G. Kresse and J. Hafner, Phys. Rev. B **47**, 558(R) (1993).

[31] I. I. Mazin, M. D. Johannes, L. Boeri, K. Koepernik, and D. J. Singh, Phys. Rev. B **78**, 085104 (2008).

[32] N. J. Ghimire, R. L. Dally, L. Poudel, D. C. Jones, D. Michel, N. Thapa Magar, M. Bleuel, M. A. McGuire, J. S. Jiang, J. F. Mitchell, J. W. Lynn, and I. I. Mazin, Sci. Adv. **6**, eabe2680 (2020).

[33] J. X. Yin *et al.*, Nature (London) **583**, 533 (2020).

[34] N. Kurita, M. Kimata, K. Kodama, A. Harada, M. Tomita, H. S. Suzuki, T. Matsumoto, K. Murata, S. Uji, and T. Terashima, Phys. Rev. B **83**, 214513 (2011).

[35] W. Uhoya, G. Tsoi, Y. K. Vohra, M. A. McGuire, A. S. Sefat, B. C. Sales, D. Mandrus, and S. T. Weir, J. Phys. Condens. Matter **22**, 292202 (2010).

[36] Y. He, T. Wu, G. Wu, Q. J. Zheng, Y. Z. Liu, H. Chen, J. J. Ying, R. H. Liu, X. F. Wang, Y. L. Xie, Y. J. Yan, J. K. Dong, S. Y. Li, and X. H. Chen, J. Phys. Condens. Matter **22**, 235701 (2010).

[37] Anupam, P. L. Paulose, S. Ramakrishnan, and Z. Hossain, J. Phys. Condens. Matter **23**, 455702 (2011).

[38] M. Nicklas, M. Kumar, E. Lengyel, W. Schnelle, and A. Leithe-Jasper, J. Phys. Conf. Ser. **273**, 012101 (2011).

[39] G. H. Cao, W. H. Jiao, Y. K. Luo, Z. Ren, S. Jiang, and Z. A. Xu, J. Phys. Conf. Ser. **391**, 012123 (2012).

[40] W. H. Jiao, Q. Tao, J. K. Bao, Y. L. Sun, C. M. Feng, Z. A. Xu, I. Nowik, I. Felner, and G. H. Cao, Epl **95**, 67007 (2011).

[41] U. B. Paramanik, P. L. Paulose, S. Ramakrishnan, A. K. Nigam, C. Geibel, and Z. Hossain, Supercond. Sci. Technol. **27**, 075012 (2014).

[42] S. Nandi, W. T. Jin, Y. Xiao, Y. Su, S. Price, D. K. Shukla, J. Strempfer, H. S. Jeevan, P. Gegenwart, and T. Brückel, Phys. Rev. B **89**, 014512 (2014).

[43] W. T. Jin, Y. Xiao, Z. Bukowski, Y. Su, S. Nandi, A. P. Sazonov, M. Meven, O. Zaharko, S. Demirdis, K. Nemkovski, K. Schmalzl, L. M. Tran, Z. Guguchia, E. Feng, Z. Fu, and T. Brückel, Phys. Rev. B **94**, 184513 (2016).

[44] S. Jiang, H. Xing, G. Xuan, Z. Ren, C. Wang, Z. A. Xu, and G. Cao, Phys. Rev. B **80**, 184514 (2009).

[45] A. Baumgartner, D. Neubauer, S. Zapf, A. V. Pronin, W. H. Jiao, G. H. Cao, and M. Dressel, Phys. Rev. B **95**, 174522 (2017).

[46] W. H. Jiao, Q. Tao, Z. Ren, Y. Liu, and G. H. Cao, Npj Quantum Mater. **2**, 50 (2017).

[47] V. H. Tran, T. A. Zaleski, Z. Bukowski, L. M. Tran, and A. J. Zaleski, Phys. Rev. B **85**, 052502 (2012).

[48] W. T. Jin, Y. Xiao, S. Nandi, S. Price, Y. Su, K. Schmalzl, W. Schmidt, T. Chatterji, A. Thamizhavel, and T. Brückel, Phys. Rev. B **100**, 014503 (2019).

[49] W. T. Jin, J. P. Sun, G. Z. Ye, Y. Xiao, Y. Su, K. Schmalzl, S. Nandi, Z. Bukowski, Z. Guguchia, E. Feng, Z. Fu, and J. G. Cheng, Sci. Rep. **7**, 3532 (2017).

[50] Z. Devizorova and A. Buzdin, Phys. Rev. B **100**, 104523 (2019).

[51] R. Prozorov and V. G. Kogan, Phys. Rev. Appl. **10**, 014030 (2018).

[52] P. Malinowski, Q. Jiang, J. J. Sanchez, J. Mutch, Z. Liu, P. Went, J. Liu, P. J. Ryan, J.-W. Kim, and J.-H. Chu, Nat. Phys. **16**, 1189 (2020).

[53] G. Adhikary, N. Sahadev, D. Biswas, R. Bindu, N. Kumar, A. Thamizhavel, S. K. Dhar, and K. Maiti, J. Phys. Condens. Matter **25**, 225701 (2013).

[54] Y. Xiao, Y. Su, S. Nandi, S. Price, B. Schmitz, C. M. N. Kumar, R. Mittal, T. Chatterji, N. Kumar, S. K. Dhar, A. Thamizhavel, and T. Brückel, Phys. Rev. B **85**, 094504 (2012).

Supplementary Information to "Strongly anisotropic antiferromagnetic coupling in EuFe$_2$As$_2$ revealed by stress detwinning"

Authors: Joshua J Sanchez[1], Gilberto Fabbris[3], Yongseong Choi[3], Yue Shi[1], Paul Malinowski[1], Shashi Pandey[2], Jian Liu[2], I.I. Mazin[5], Jong-Woo Kim[3], Philip Ryan[3,4], Jiun-Haw Chu[1*]

Affiliation:

[1] Department of Physics, University of Washington, Seattle, Washington 98195, USA.

[2] Department of Physics and Astronomy, University of Tennessee, Knoxville, Tennessee 37996, USA.

[3] Advanced Photon Source, Argonne National Laboratories, Lemont, Illinois 60439, USA.

[4] School of Physical Sciences, Dublin City University, Dublin 9, Ireland.

[5] Department of Physics and Astronomy and Quantum Science and Engineering Center, George Mason University, Fairfax, VA 22030

*Correspondence to: jhchu@uw.edu (J.-H.C)

(Dated: 8/9/2021)

I. XMCD Measurement

The XMCD measurement uses a circularly polarized incident x-ray beam and measures the helicity-dependent intensities $\mu_{R,0}$ and $\mu_{L,0}$ as a function of x-ray energy. To analyze these data, we first sum $\mu_{R,0}$ and $\mu_{L,0}$ and normalize by the jump in intensity at the L3 edge. Then we correct the data for self-absorption to get μ_R and μ_L. In this case the XAS is the sum of the two intensities, $\mu_R + \mu_L$, and is found to peak at E=6.975 keV, i.e. at the peak of the Eu L3 edge as expected. The difference in intensity $\mu_R - \mu_L$ is the XMCD and is peaked at E=6.973 keV. Hence, the XMCD is already normalized by the total intensity.

During the initial calibration it was found that the sample was not appreciably displaced by applied field up to 1T; this means the same sample volume was probed by the XMCD measurement over the whole field range. For this reason, it was unnecessary to do a full energy scan at every field point. Instead, a much quicker measurement was performed using x-rays of energy E=6.970 keV, just below the XMCD peak but with roughly half the peak intensity. At each field point the helicity-dependent intensity measurement was made. At the maximum field value of $\pm$1T a full energy scan was performed and used to normalize the E=6.970 keV data vs field by the peak XMCD value at 1T and E=6.973 keV.
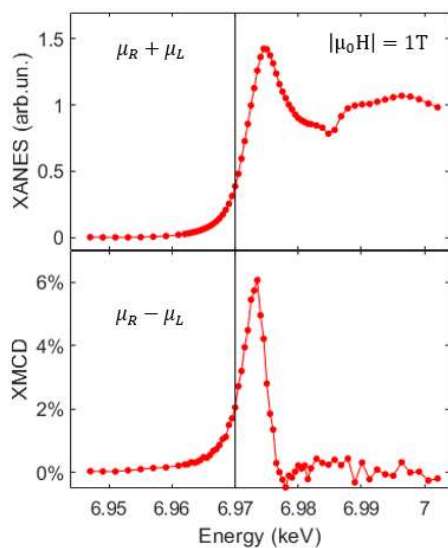
Fig.S1. XANES and XMCD. Energy scan of incident x-rays of left and right helicity (normalized intensity μ_L and μ_R, respectively) at a fixed applied field of 1T and at T=7K for the B domain (i.e. saturated magnetic moment post spin flip). The sum of the helicity intensities yields the XANES (arbitrary units) while the normalized difference yields the XMCD. Line shows energy at which field-dependent intensity scans were made.

II. Strain detwinning

At T=7K, the EuFe$_2$As$_2$ orthorhombicity $\left(\varepsilon = \frac{a-b}{a+b} \right)$ is approximately 0.28%, while the maximum nominal strain (ε_{xx}^{nom}) applied to the sample is 0.3%. Naively we would expect to fully detwin the sample. However, as discussed in ref. [24], pinned remnant domains persist up to large applied strains, inhibiting a total detwinning. We can estimate the A domain population vs applied strain using calibration data from refs. [24,53], where the uniaxial strain detwinning was monitored with simultaneous x-ray diffraction. In Figure S2 we show simulated detwinning data for EuFe$_2$As$_2$, adjusting the detwinning for the difference in sample orthorhombicity. We find that at our maximum applied strain (grey bars) that the sample volume should contain about 5% of the minor domain. Evidence for this remnant domain is visible in the small resistivity drop of the A domain at 7K (Figures 3a and 4b of the main text).
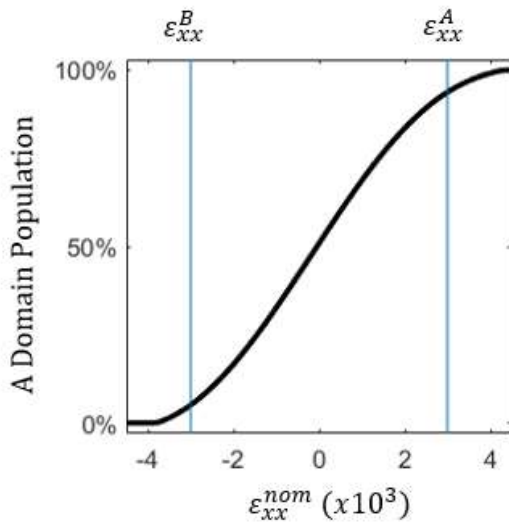

Fig. S2 Simulated detwinning data for EuFe$_2$As$_2$ at T=7K based on x-ray diffraction detwinning data from ref. [24]. Grey bars indicate the strains applied to create the A and B monodomains of Figure 3 in the main text.

III. Fixed-length twinned sample prevented from field detwinning

Here, we demonstrate that the sample can be tuned to an arbitrarily twinned state and undergoes the spin flip/canting transitions without field detwinning and without a change in the critical field values. The sample was strain tuned to a state with approximately equal proportion of A and B domains while at 7K, and then run through the same field loop as the data measured in the fully detwinned states presented in Figure 3. (XMCD data was not collected for the first 0 to 0.6T range of the field sweep). Figure S3a shows the XMCD and resistivity of the twin domain state (green) compared to the detwinned A and B domain data from Figure 3. The resistivity returns to its zero-field value after the field loop, suggesting that no persistent field detwinning occurs. In Figure S3b we plot the absolute value of the XMCD and the magnetoresistance of the twin domain state against a linear combination of 51% A domain and 49% B domain data from Figure 4a. We find the linear combination is an extremely good match to the measured data, with $R^2 > 0.97$ and $R^2 > 0.99$ for the XMCD and magnetoresistance, respectively (Fig. S3b, black). This indicates the twinned state is indeed in a nearly equal domain population state at zero field, which is maintained over the applied field range, and each domain responds nearly identically to field as in the fully detwinned state. Further, this shows that the detwinning strains applied in this work do not meaningfully alter the critical fields H_A^{sat} and H_B^{flip}.

The behavior of the twinned sample held in the strain cell is in sharp contrast with the freestanding sample (i.e. one not encased in epoxy). We measured the magnetoresistance of a freestanding sample in a Quantum Design PPMS at 7K with field applied perpendicular to current and in-plane at 10 degrees above grazing incidence, identical to the conditions of the strained sample. For a freestanding crystal in an initial zero-field equal A/B domain population state, an applied field in this geometry would first detwin the sample towards the lower resistivity A domain followed by a rapid detwinning to the higher resistivity B domain [14,16,17]. This manifests in our freestanding sample as an

initial decrease of the resistivity at low field followed by a sudden jump at $\mu_0 H = 0.44T$, with a large

hysteresis across the loop and a lower resistivity value on return to zero field indicating the persistent

domain detwinning (Fig.S3b, violet). This clear difference in behavior from the fixed strain sample further

corroborates that fixed strain prevents field detwinning and so the resulting magnetoresistance can be

interpreted as purely the consequence of Eu moment reorientation [17,18,54].
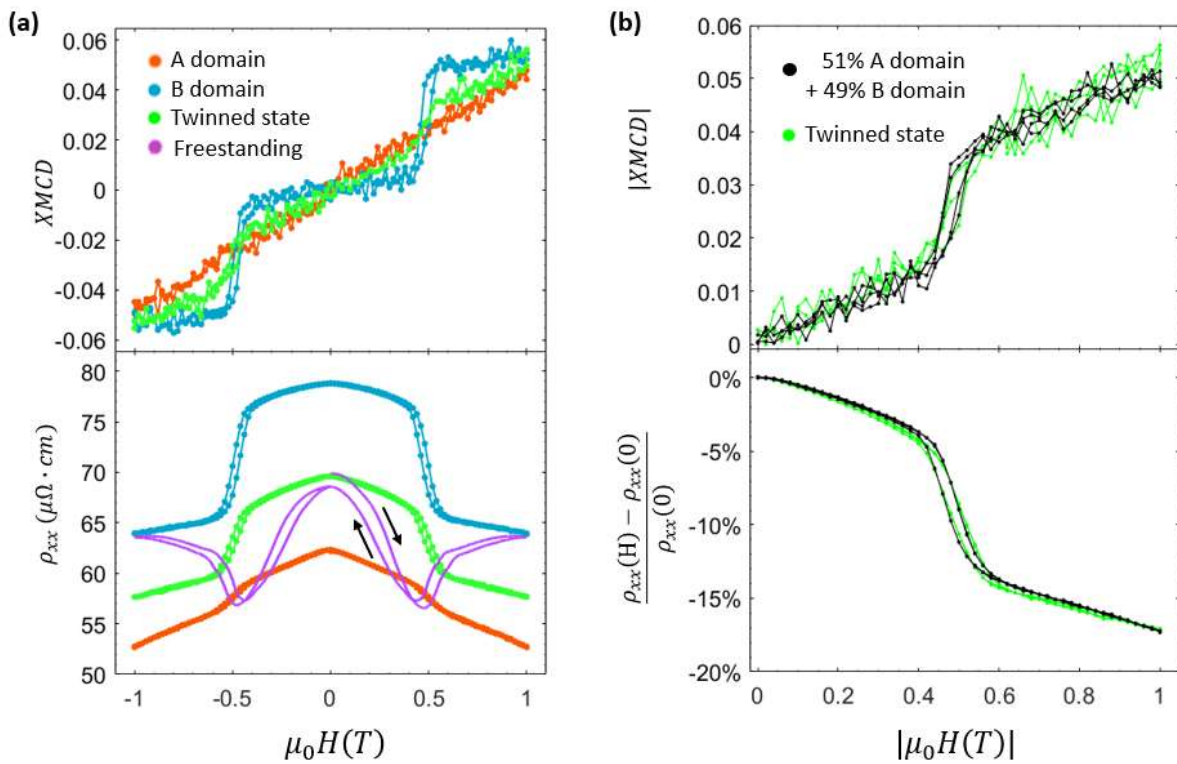

Fig. S3 (a) Data from Fig.3a-b for A (orange) and B (blue) detwinned monodomains, as well as a nearly-

zero strain twin domain state (green) run through the same field loop. Resistivity from a second

freestanding sample (violet) shows a substantially different field response to the fixed length sample

due to hysteretic domain detwinning. (b) Twin domain data (green) with a linear superposition of 51% A

domain and 49% B domain data superimposed (black) (absolute value of XMCD across field sweeps).

IV. Spin Hamiltonian derivation

We refer the reader to ref. [14] for a detailed discussion of the spin Hamiltonian in this system. We briefly review the main results here and expand upon them with the inclusion of an Eu-Eu anisotropic exchange term W. Considering the doubled unit cell of the fully ordered state ($Eu_2Fe_4As_4$), and a fixed Fe moment orientation aligned along $\hat{x}$ (Fig.S4), the magnetic energy is given by

$$E = 2J_x e_{1x} e_{2x} + 2J_y e_{1y} e_{2y} + 8K \sum_i (\vec{e_i} \cdot \hat{y})^2 - M \sum_i \vec{H} \cdot \vec{e_i}$$

where $\vec{e_i} = (e_{ix}, e_{iy})$ is the unit vector of the ferromagnetic moment of the Eu atoms in the 2 AFM sublattices, $(\vec{e_i} \cdot \hat{y})^2$ is the biquadratic interaction between Eu and Fe moments (with interaction energy K for each of the 8 Fe nearest neighbors to each Eu moment), $\vec{H}$ is the applied field with isotropic coupling to the Eu moments (the moment size M of each Eu AFM sublattice is approximately 6.8 μ_B at T=7K), and the summations are over the two Eu planes. The anisotropic coupling energy between the Eu AFM sublattices is directionally dependent, with $J_x = J + W$, $J_y = J - W$, and $W = W(M_{i,x} M_{i+1,x} - M_{i,y} M_{i+1,y})$, where $M_{i,x}$ and $M_{i,y}$ are the x and y components of the Eu moment in the ith layer. In the initial zero field case (Fig. S4a) we have $\vec{e_1} = \hat{x}$, $\vec{e_2} = -\hat{x}$, and $E = -2J_x$.

We consider the evolution of the energy with a magnetic field applied along the 3 directions used in the main experiment by symmetrizing the Eu moments about the field direction. First defining $\vec{e_1} = \cos\theta\ \hat{x} + \sin\theta\ \hat{y}$ in all cases, we define $\vec{e_2} = -\cos\theta\ \hat{x} + \sin\theta\ \hat{y}$ for $\vec{H} = H\hat{y}$ (Fig.S2b), $\vec{e_2} = \cos\theta\ \hat{x} - \sin\theta\ \hat{y}$ for $\vec{H} = H\hat{x}$ (Fig.S4c), and $\vec{e_2} = \sin\theta\ \hat{x} + \cos\theta\ \hat{y}$ for $\vec{H} = H\left(\frac{1}{\sqrt{2}}\hat{x} + \frac{1}{\sqrt{2}}\hat{y}\right)$ (Fig.S4d). By substituting these moment definitions into the spin Hamiltonian, minimizing the energy with respect to θ, and then solving for a fully saturated moment ($\theta = \frac{\pi}{2}$, 0, and $\frac{\pi}{4}$, respectively) we arrive at the saturation fields:

$$H_A^{sat} = \frac{4J + 16K}{M}$$

$$H_B^{flop,sat} = \frac{4J - 16K}{M}$$

$$H_{AB}^{sat} = \frac{4J}{M}.$$

From the form of these saturation fields, it is clear that the anisotropy between J_x and J_y are averaged over, resulting in the isotropic J and no explicit term W. However, the term $H_B^{flop,sat}$ refers to the saturation field after a spin flop transition (which onsets at $H_B^{flop,onset} = \frac{8}{M}\sqrt{K(J - 4K)}$ for $W = 0$), while a key finding of our measurement is that a sharp spin flip transition occurs instead. Treating this transition as an Ising spin flip, we have

$$H_B^{flip} = \frac{2J_x}{M} = \frac{2(J + W)}{M}.$$

For a spin flip transition to occur, the energy at the transition must be lower than the fully-saturated spin flop phase, $E(H_B^{flip}) < E(H_B^{flop,sat})$. Solving for each energy results in the condition

$$\frac{J}{8K + W} < 1.$$

As discussed in the main text, from our measurements of H_A^{sat}, H_B^{flip} and $H_{45°}^{sat}$, our experimentally determined values of J, W, and K result in the spin flip condition being satisfied.
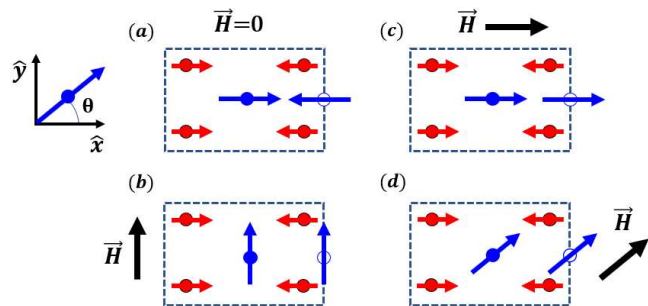
Fig. S4 The 4 Eu-Eu moment arrangements relative to a fixed Fe moment arrangement, with (a) Eu AFM along $\hat{x}$, (b) Eu FM along $\hat{y}$, (c) Eu FM along $\hat{x}$, and (d) Eu FM along $\frac{1}{\sqrt{2}}(\hat{x} + \hat{y})$.